

ER9 车轮材料激光熔覆层微观组织及性能研究

杨文斌^{1,2}, 李仕宇¹, 肖乾^{1*}, 杨春辉¹, 陈道云¹, 廖晓咏¹¹华东交通大学轨道交通基础设施性能检测与保障国家重点实验室, 江西 南昌 330013;²浙江师范大学城市轨道交通智能运维技术与装备重点实验室, 浙江 金华 321005

摘要 为提高 ER9 车轮材料的表面强度和耐蚀耐磨性, 延长车轮的服役寿命, 本团队选择在激光熔覆中应用最广泛的铁基、镍基和钴基三种自熔性合金粉末为熔覆材料, 在 ER9 车轮钢表面进行激光熔覆试验。通过相关试验评价熔覆层的微观组织、力学性能、摩擦磨损性能和耐蚀性。结果表明: 车轮钢表面激光熔覆层的显微组织均为枝晶组织和共晶组织, 且组织致密均匀, 与基体实现了良好的冶金结合。熔覆层的硬度显著提升, 镍基合金熔覆层具有良好的拉伸强度和冲击韧性, 断口呈韧性断裂特征; 钴基和铁基合金熔覆层的断裂方式为脆性断裂, 力学性能差异不明显。相较于基体, 熔覆层具有较低的摩擦因数、磨损率与更优的耐蚀性, 其中钴基合金熔覆层的硬度较高(显微硬度相比基体提高了 72.8%), 耐磨性最优(摩擦因数为 0.31, 磨损量为 4 mg 和磨痕深度为 10.70 μm), 耐蚀性最好(阻抗值比基体高 2 个数量级)。镍基熔覆层磨损面较为粗糙且磨损率较大, 减磨效果不佳, 硬度和强度较弱; 尽管相比铁基涂层, 钴基涂层的耐磨性和耐蚀性显示出了一定优势, 但前者的工程成本较低, 综合效果更好。

关键词 激光技术; 车轮材料; 激光熔覆; 合金粉末; 微观组织; 力学性能; 耐磨性; 耐蚀性

中图分类号 TG174.4

文献标志码 A

DOI: 10.3788/CJL221093

1 引言

随着我国列车速度的提高以及轴重、运量的增大, 轮轨间运行环境变得更加复杂, 车轮表面常常会因磨损、腐蚀、强度下降以及疲劳开裂等出现严重损伤、疲劳和断裂破坏等, 极大地影响了行车的安全性和旅客的舒适度^[1]。为了消除车轮表面缺陷, 目前常用镟修工艺进行修型, 这将造成材料浪费与经济损失。据统计, 我国每年投入多达 80 亿元用于轮轨的维护与更新^[2]。为了提高车轮的服役寿命, 亟须开展提高车轮表面强度和耐蚀性、耐磨性的研究。

目前, 主要的金属表面处理技术有超声冲击^[3]、激光冲击^[4]、激光淬火^[5]、层流等离子淬火^[6]、激光熔覆^[7]等。与其他表面强化技术相比, 激光熔覆技术制备的涂层可与基材形成良好的冶金结合, 而且涂层厚度和稀释率可控, 涂层组织均匀细小。选择不同的材料进行激光熔覆可以实现高强度以及耐磨、耐蚀等性能优良的涂层。目前, 已有很多学者通过在轮轨表面制备激光熔覆层来提高其抗损伤能力, 并在此方面进行了大量研究^[8-9]。慕鑫鹏等^[10-11]在车轮钢基材上激光熔覆了铁基和钴基合金涂层, 对滚试验后发现两种涂层均呈现出了良好的耐磨效果, 磨损率相较于基材降低了

80% 以上。丁阳喜等^[12-13]在轮轨表面熔覆了铁基涂层和铁、钴复合基涂层, 这两种涂层表现出了比车轮钢基体材料更加优异的摩擦磨损性能和滚动接触疲劳性能。Guo 等^[14]在 CL60 车轮钢表面熔覆了钴基合金涂层并通过滚动试验机来测试其耐磨性, 结果发现强化后的表面磨损率相比车轮钢基体下降了 42.2%~69.4%。这一结果表明激光熔覆技术可用于车轮损伤修复, 有效提高了车轮材料的耐磨性。Ding 等^[15]通过滚动摩擦磨损试验考察了铁基合金涂层的性能, 结果显示, 该涂层对降低熔覆层的摩擦因数具有积极作用。Wang 等^[16]在轮轨材料表面熔覆了铁基合金涂层, 该涂层提高了轮轨材料的耐磨性及耐滚动接触疲劳性能。Ringsberg 等^[17]采用数值分析方法和相关试验研究了 Co-Cr 合金熔覆层的耐磨性, 结果显示, 涂层表面不易产生棘轮效应而且能够避免出现滚动接触疲劳损伤。Lewis 等^[18]采用激光熔覆技术在钢轨材料表面制备了高性能马氏体不锈钢涂层(MSS), 测试后发现激光熔覆处理的钢轨试样的疲劳性能显著提高, 同时车轮材料的磨损也得以减轻。Zhu 等^[19]通过滚动接触试验研究了受损车轮表面不锈钢涂层的疲劳性能和耐磨性, 结果显示, 不锈钢涂层表现出了比车轮基体材料更优异的疲劳强度和耐磨性。这一结果说明激光熔覆技

收稿日期: 2022-08-01; 修回日期: 2022-08-25; 录用日期: 2022-09-15; 网络首发日期: 2022-09-28

基金项目: 江西省自然科学基金(20202BABL214028)、江西省教育厅科学技术研究项目青年项目(GJJ180344)、江西省研究生创新专项项目(YC2021-S462, YC2021-S465)

通信作者: *jxralph@foxmail.com

术可用于损伤车轮的强化。分析后可以发现,以上研究主要集中于车轮表面激光熔覆层的滚动接触疲劳性能,而针对熔覆后车轮钢力学性能、耐磨性及耐蚀性能的研究较为欠缺。

自熔性合金粉末具有良好的自脱氧造渣功能^[20]以及制备简单、成形性能优异等特征,鉴于此,本团队采用激光熔覆技术在 ER9 车轮材料表面分别制备出激光熔覆领域应用广泛的铁基合金熔覆层、镍基合金熔覆层和钴基合金熔覆层,并对熔覆层的显微组织、力学性能、耐磨性以及耐蚀性等展开研究,以揭示基体和熔覆层的力学性能、损伤机制和腐蚀行为。本研究成果可为激光熔覆技术在轨道车轮表面强化领域的应用提供重要的理论支持。

2 试 验

2.1 材 料

激光熔覆试验的基体材料取自列车车轮(ER9 车轮钢)踏面,其化学成分如表 1 所示。用线切割切取尺寸为 130 mm×50 mm×30 mm 的钢块若干个。激光

表 1 ER9 的化学成分
Table 1 Chemical composition of ER9

Element	Mass fraction /%
C	0.6
Si	0.4
Mn	0.8
P	0.02
S	0.015
Cr	0.3
Mo	0.08

熔覆试验前,先采用普通砂纸(120 目)对基体材料进行打磨,以去除其表面的氧化膜,然后用乙醇进行擦拭,以清洁其表面。熔覆材料分别为清河县兴荣源金属材料有限公司生产的铁基合金粉末、长沙天久金属材料有限公司生产的镍基合金粉末和北京首一喷涂技术有限公司生产的钴基合金粉末,它们的化学成分如表 2 所示。

表 2 粉末材料的化学成分
Table 2 Chemical composition of powder materials

Powder	Mass fraction /%								
	C	W	Ni	B	Mo	Fe	Cr	Si	Co
Co-based powder	0.9-1.2	4.0-4.8	3.0			3.0	27.5-29.5	0.9-1.3	Bal.
Fe-based powder	0.8-1.2		9-12	3.8-4.2		Bal.	16-18	1.0-2.0	
Ni-based powder	0.02		Bal.		8.89	0.29	21.55	0.096	0.03

2.2 熔覆工艺及制样

采用 LaserlineLDF6000-100 激光柔性增材制造系统在试样表面以同轴送粉方式制备厚度约为 15 mm 的熔覆层。设计并优化的激光工艺参数如下:激光功

率 1.6 kW,扫描速度 7.5 mm/s,光斑直径 4 mm,搭接率 50%。整个熔覆过程在氩气(纯度大于 99.9%)保护下按纵向“弓”形路径进行。最后,利用线切割方法取样,熔覆过程示意图、取样方式及试样尺寸如图 1 所示。

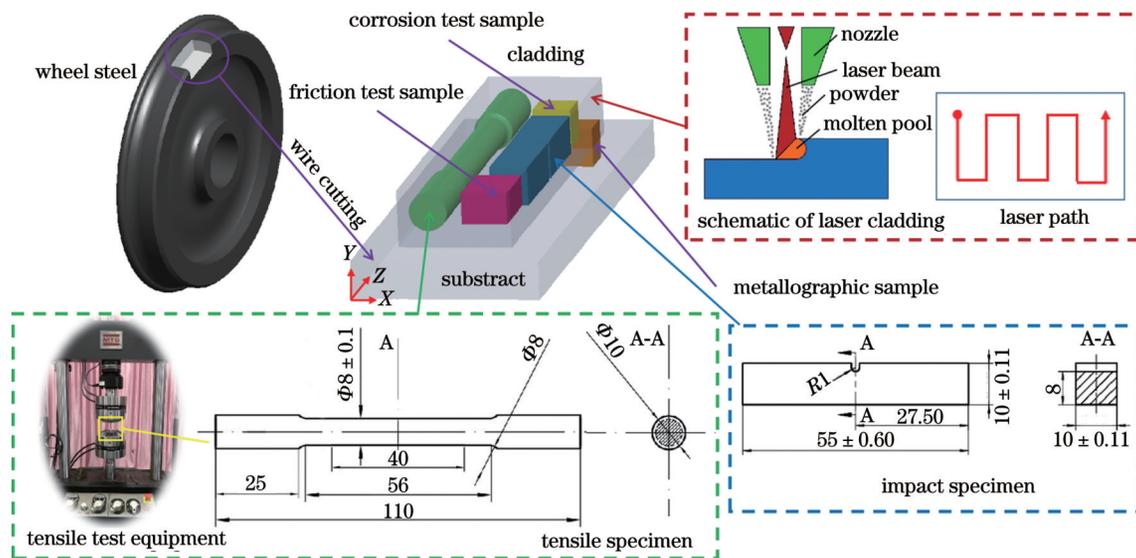


图 1 试样熔覆过程、取样方式及试样尺寸示意图

Fig. 1 Schematic of sample cladding process, sampling and sample size

2.3 测试与分析

沿垂直于扫描速度方向的熔覆层横截面切割出尺寸为 10 mm×8 mm×10 mm 的样品,制备金相试样,对金相试样进行打磨、抛光后用王水(HCl与HNO₃按体积比为 3:1 混合配制而成)进行腐蚀,采用 SU8010 扫描电子显微镜(SEM)对试样的微观组织进行观察。采用 X 射线衍射(XRD)技术对熔覆层进行物相分析。利用维氏硬度仪(Qness-Q60)测量试样的显微硬度。

采用 MTS 万能试验机,根据 GB/T 228.1—2010《金属材料 拉伸试验 第 1 部分:室温试验方法》的要求进行拉伸测试;冲击试验参考 GB/T 229—2007《金属材料 夏比摆锤冲击试验方法》制备标准 U 形缺口夏比摆锤冲击试样,拉伸与冲击试验的取样部位以及试样规格如图 1 所示。为保证测试数据的准确性,每组取 3 个试样,取 3 次测试的平均值作为最终的测试值。采用 SEM 观察拉伸与冲击试验后试样的断口形貌。

摩擦磨损试样的尺寸为 20 mm×15 mm×10 mm。对激光熔覆样品表面进行磨削、抛光,使熔覆层表面平整,表面粗糙度为 0.05~0.1 μm。摩擦磨损试验采用 MFT-EC4000 试验仪进行,对磨件为 Φ6 mm 的 Si₃N₄ 陶瓷球(硬度为 1700 HV,表面粗糙度 R_a≤0.2 μm),固定载荷为 20 N,往复频率为 2 Hz,摩擦距离为 5 mm,

摩擦时间为 60 min。试验后,用乙醇对所有样品进行 15 min 的超声波清洗。借助 SEM 及其附带的能谱仪(EDS)对试样进行表征分析。使用精度为 0.1 mg 的电子天平对磨损前后的试样进行称重,取 6 次称重的平均值计算磨损量。

在室温 3.5%NaCl 溶液中,利用电化学工作站测试样品的动电位极化曲线(Tafel)与电化学阻抗谱(EIS)。采用标准的三电极体系,其中熔覆层和基体试样为工作电极,饱和甘汞(内充饱和 KCl 溶液)为参比电极,Pt 作为辅助电极,暴露面积为 1 cm²。电化学阻抗谱测试频率范围为 0.01~10⁵ Hz,振幅为 10 mV,随后以 1 mV/s 的扫描速率完成动电位极化测试。特别地,在阻抗谱和动电位极化测试前,需测试 20 min 的开路电位(OCP),直至腐蚀电位稳定。

3 结果与讨论

3.1 微观组织

图 2 为激光熔覆层截面各部分的微观组织。在 3 种熔覆层的截面上可以观察到 3 个不同的区域,即熔覆层、热影响区和基体。熔覆层表面组织致密,未发现气孔、裂纹等缺陷;基体与熔覆层之间存在一条清晰的分界线(熔合线),这种分界线是材料形成优异冶金结合的重要特征^[21]。熔合线位于熔覆层与基体的过渡区

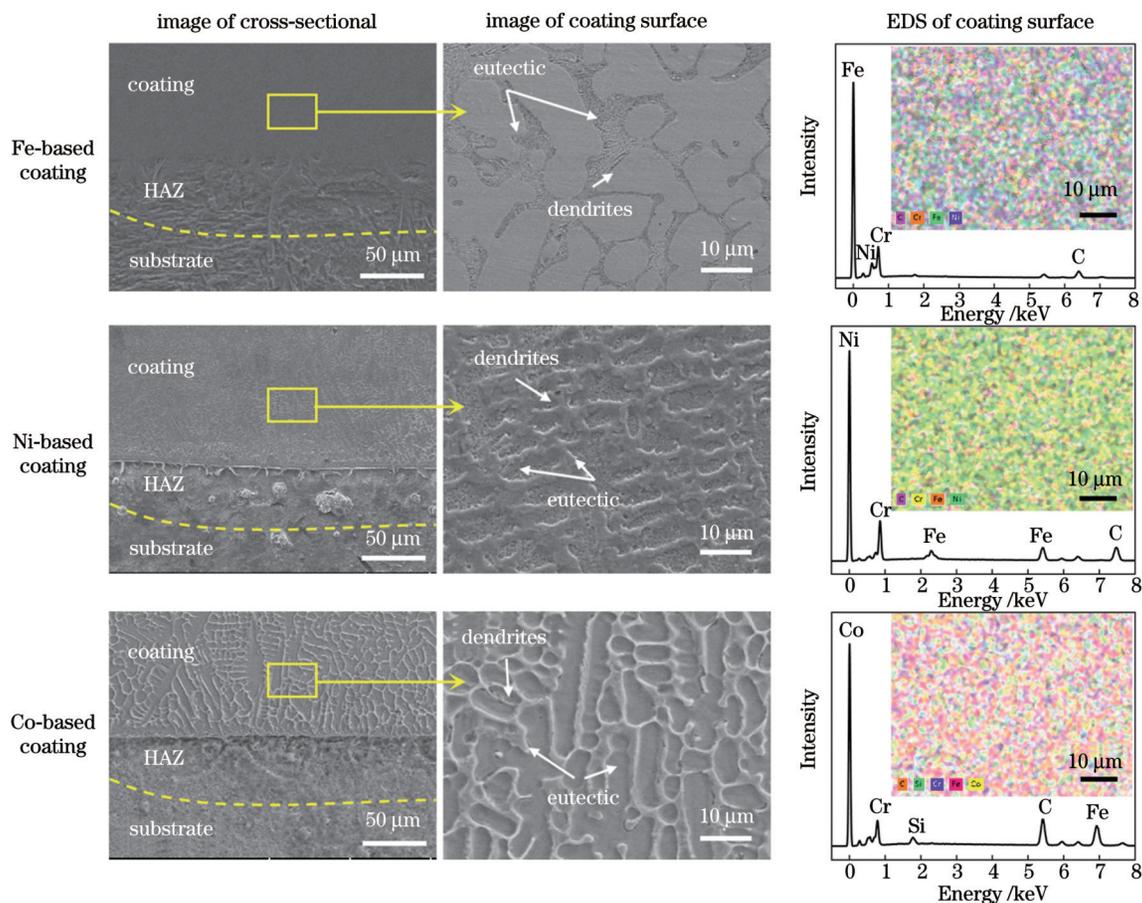


图 2 激光熔覆层的微观组织与能谱分析

Fig. 2 Microstructures and energy spectra analysis results of laser cladding coating

域,具有良好的相容性,可以提升材料的结合强度。此外,在熔池底部至表面方向上出现了垂直于熔合线方向生长的晶体组织^[22]。由快速凝固理论可知,影响熔覆层组织特征的主要因素为温度梯度(G)和凝固速率(R),二者的比值(G/R)决定了微观组织的形貌^[23]。高倍 SEM 图片是熔覆层中部区域的显微组织,各熔覆层的显微组织均为枝晶组织和共晶组织。主要原因是熔融金属在激光熔覆快速冷却凝固过程中形核析出后长大形成枝晶,随后晶间液相快速凝固逐渐形成密集的共晶组织(共晶形貌由凝固速率决定^[24-25])。

从熔覆层表面的元素分析及元素定量能谱分析结果可以看出:铁基熔覆层中主要存在 Fe、Cr、Ni、C 元素,其中 Cr、C 元素在枝晶间富集,该现象是凝固时晶型转变控制的结果^[26];镍基熔覆层主要以 Ni 和 Cr 元素为主,并且溶解了 Fe 和 C 等元素,涂层内元素分布均匀,未发现明显的富集现象;钴基熔覆层中的主要元素为 Co、Cr、Fe 和 C 等,枝晶上和枝晶内的元素分布不一,枝晶上有 Cr、C 元素富集,Fe 元素主要分布在枝晶内。

图 3 为铁基、镍基和钴基熔覆层的 XRD 谱。由铁基熔覆层的 XRD 谱分析可以看出铁基熔覆层主要由 α -Fe、(Fe, Ni)、 Cr_7C_3 等固溶体组成。在激光熔覆的快速凝固过程中,随着温度逐渐降至室温,奥氏体(γ -Fe)转变成铁素体(α -Fe),同时保留了部分残余奥氏体。Fe 和 Ni 元素易结合形成 (Fe, Ni) 固溶体, (Fe, Ni) 相可以提高熔覆层的耐磨性。熔覆层中的 C 与 Cr 易形成 Cr_7C_3 碳化物,此碳化物有助于增强涂层的硬度和强度^[27]。从镍基熔覆层的 XRD 谱可知镍基熔覆层由固溶体 γ -Ni、硬质相 $Cr_{23}C_6$ 和金属间化合物 $FeNi_3$ 组成。液态合金首先通过匀晶转变生成 γ -Ni 固溶体, γ -Ni 固溶体可以提高涂层的表面强度且具有一定的塑性。涂层中过量的 Ni 元素不发生共析反应,最终生成 $FeNi_3$ 相。合金粉末中的大量 Cr 与元素 C 发生反应生成硬质相 $Cr_{23}C_6$, 硬质相 $Cr_{23}C_6$ 可对位错运动和晶界迁移起到减缓作用从而产生弥散强化,有利于提升熔覆层的

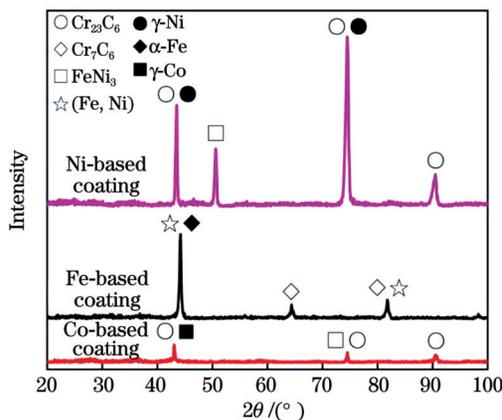


图 3 激光熔覆层的 XRD 谱
Fig. 3 XRD spectra of laser cladding coating

硬度和耐磨性^[28]。从钴基熔覆层的 XRD 谱可以看出钴基熔覆层的结晶相主要是 $FeNi_3$ 相、 γ -Co 相和 $Cr_{23}C_6$ 相,其中 γ -Co 是多种元素的钴基固溶体。在激光熔覆的快速熔化凝固过程中,Co 元素形成 γ -Co,之后随着温度快速下降, γ -Co 相未能及时发生相变而保留下来^[29]。Cr 与元素 C 发生反应生成高铬碳化物 $Cr_{23}C_6$, $Cr_{23}C_6$ 是激光熔池凝固冷却过程中形成的介稳相,可以起到提高耐磨性的作用^[30]。

3.2 熔覆层的力学性能

图 4 为三种熔覆层试样的显微硬度分布。由图 4 可知熔覆层内部的硬度曲线无较大波动起伏,从熔覆区到热影响区再到基材,硬度的总体趋势是呈台阶式逐渐降低。基材的显微硬度约为 263.9 HV;铁基熔覆层的平均显微硬度最高可达 716.5 HV,是基体的 2.7 倍;镍基和钴基熔覆层的硬度分别约为 384.2 HV 和 456.1 HV,与基材相比分别提高了 45.6% 和 72.8%。这表明激光熔覆处理可以较大程度地提高金属的表面硬度。结合前面的微观组织和物相分析可知涂层能获得高硬度的主要原因是熔覆层中的元素在冷却凝固过程中于晶界处偏析形成了固溶体和高硬度碳化物,产生了强化效果,增强了涂层组织的硬度^[31]。与熔覆层相比,热影响区的硬度呈现下降趋势。这是因为熔覆层与基体之间的界面处存在合金元素稀释现象,致使热影响区的显微硬度大幅度降低,但仍然高于基材。同时,熔覆层与基体过渡区的硬度处于涂层与基材之间,说明界面实现了良好的冶金结合,有利于防止熔覆层脱落。

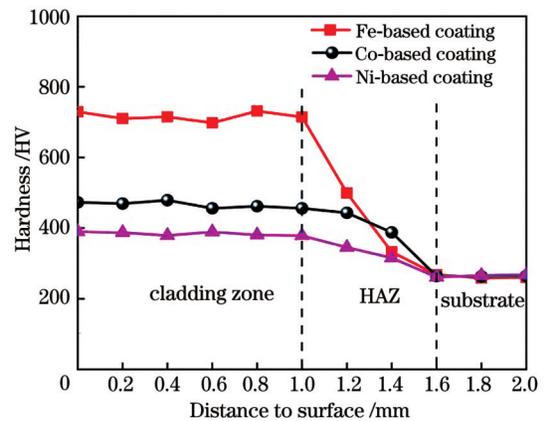


图 4 激光熔覆层横截面的硬度分布
Fig. 4 Hardness distribution of laser cladding coating cross section

熔覆层试样的拉伸性能是评价熔覆层成形质量的一个重要指标,图 5 给出了不同激光熔覆层试样的拉伸性能。由图 5(a)可见,镍基熔覆层试样拉伸后出现了明显的颈缩,断口位于中部,断口倾斜角度大,而铁基和钴基熔覆层试样的颈缩不显著,断口较为整齐。分析应力-应变曲线可以发现镍基熔覆层试样出现了明显的屈服阶段,而铁基和钴基熔覆层试样表现出了

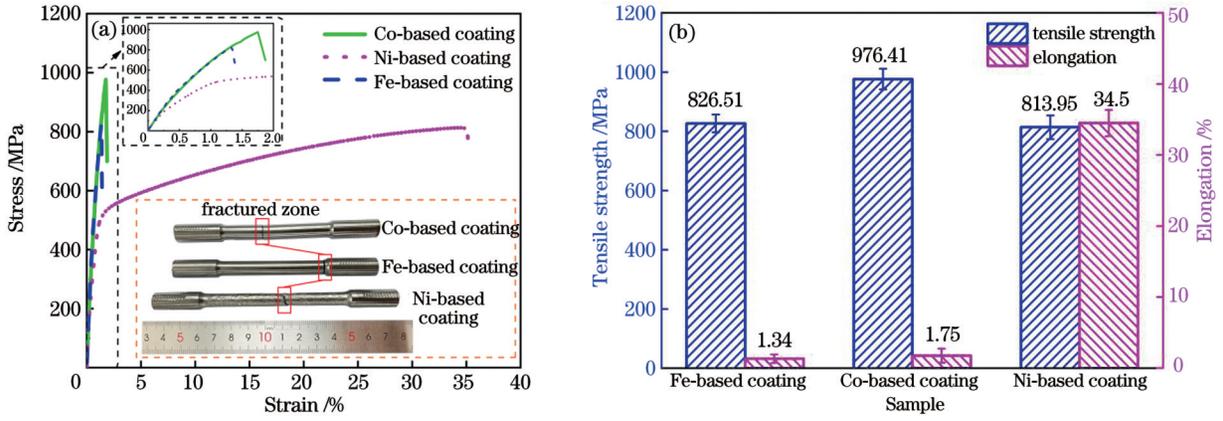


图 5 熔覆层试样的拉伸性能。(a)应力-应变曲线图;(b)抗拉强度与伸长率

Fig. 5 Tensile properties of laser cladding coating samples. (a) Stress-strain curve graph; (b) tensile strength and elongation

与镍基熔覆层试样完全不同的特性,即铁基和钴基熔覆层试样在未发生塑性屈服现象的情况下被拉断,说明其断裂形式为脆性断裂。微观组织的不同最终导致材料的使用性能各不相同^[32]。铁基熔覆层拉伸试样的伸长率最低,仅为1.34%,如图5(b)所示,说明其塑性较差;钴基熔覆层试样的抗拉强度最大,约为976.41 MPa,该值相较于文献^[33]所述车轮钢基材的抗拉强度(约881.8 MPa)提高了10.7%;镍基熔覆层拉伸试样的抗拉强度约为813.95 MPa,但其伸长率达到了34.5%,表明镍基熔覆层试样具有良好的延展性。

为了明晰各熔覆层试样在室温下的断裂机制,用乙醇对断口进行超声清洗,然后进行SEM观察,各试样的断口形貌如图6所示。观察低倍断口形貌可以发现铁基和钴基熔覆层试样断口表面无明显的塑性变形。观察高倍断口形貌可以发现:铁基熔覆层试样拉伸断口上存在由解理面形成的解理台阶;钴基熔覆层试样拉伸断口上呈现出典型的河流花样特征,表现为脆性断裂;镍基熔覆层试样拉伸断口上出现了大小不一的韧窝状形貌,呈现出韧性断裂特征,其塑性是三种试样中最高的。

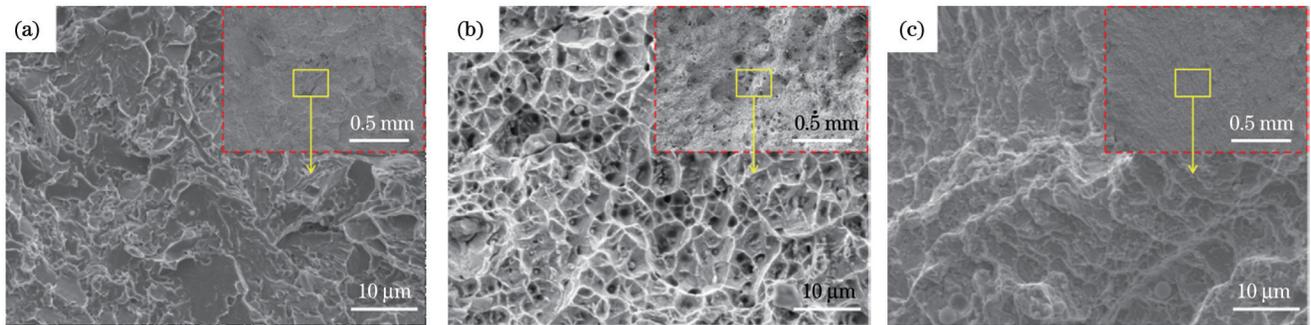


图 6 试样的拉伸断口形貌。(a)铁基熔覆层试样;(b)镍基熔覆层试样;(c)钴基熔覆层试样

Fig. 6 Tensile fracture morphologies of samples. (a) Fe-based laser cladding coating sample; (b) Ni-based laser cladding coating sample; (c) Co-based laser cladding coating sample

图7为三种熔覆层试样的冲击性能。铁基、钴基和镍基熔覆层试样的冲击韧度 α_k 分别约为2.44、6.63、163.56 J/cm²。对比后发现铁基和钴基熔覆层试样的冲击韧性远低于车轮钢基材(约29.25 J/cm²)^[33]和镍基熔覆层试样,这表明激光熔覆试样在提高硬度的同时脆性也增大了,相应的冲击韧性大幅降低^[34]。各熔覆层试样的冲击断口形貌如图8所示,可见:铁基和钴基熔覆层试样断口呈现出高低不平的形貌,并存在大量撕裂棱和台阶,断口上存在脆性区;镍基熔覆层试样断口上存在细小而密集的韧窝,韧性断裂特征明显。镍基熔覆层试样断口上的这些韧窝通常都会长大,连接起来后就会形成裂纹,导致试样发生微孔聚集型断裂^[35]。

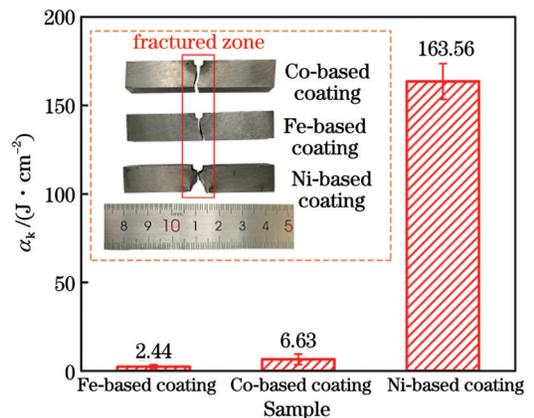


图 7 试样的冲击韧性

Fig. 7 Impact toughness of samples

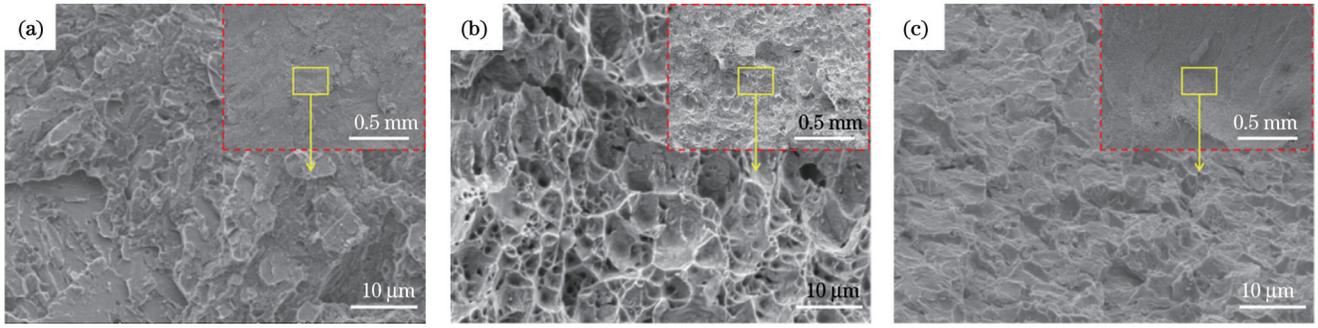


图 8 试样的冲击断口形貌。(a)铁基熔覆层试样;(b)镍基熔覆层试样;(c)钴基熔覆层试样

Fig. 8 Impact fracture morphologies of samples. (a) Fe-based laser cladding coating sample; (b) Ni-based laser cladding coating sample; (c) Co-based laser cladding coating sample

3.3 熔覆层的耐磨性

图 9(a)显示了基体和激光熔覆层试样进行摩擦磨损试验时摩擦因数的变化。由图 9(a)可知,试样的摩擦过程主要分为跑合阶段和稳定磨损阶段。在跑合初期,摩擦磨损过程本质上是熔覆层表面的凸出体与陶瓷球接触,二者的实际接触面积非常小,因此存在较大的局部接触应力,接触区的微凸体被挤压、剪切后剥落形成大量磨粒,试样表面变得粗糙,摩擦因数急剧上升且波动明显^[36]。经过跑合后,各熔覆层的摩擦因数约在 20 min 后趋于平稳,基体的摩擦因数稳定在 0.36 左右,钴基合金熔覆层的摩擦因数稳定在 0.31 左右,铁基和镍基熔覆层的摩擦因数分别稳定在 0.32 和 0.34 左右。图 9(b)为车轮钢基体和熔覆层的磨损量、磨损

率对比图。磨损率^[37]的计算公式为

$$W_r = \frac{\Delta M}{F \times L}, \quad (1)$$

式中: W_r 为磨损率,单位为 $\text{g}/(\text{N}\cdot\text{m})$; ΔM 为试样的质量损失,单位为 g ; F 为载荷,单位为 N ; L 为摩擦总往复行程,单位为 m 。基体的磨损量和磨损率均最高,分别约为 19 mg 和 $1.9 \times 10^{-4} \text{ g}/(\text{N}\cdot\text{m})$ 。经激光熔覆处理后,磨损量和磨损率均有不同程度的降低,其中:钴基合金熔覆层的磨损量和磨损率最低,分别为 4 mg 和 $0.4 \times 10^{-4} \text{ g}/(\text{N}\cdot\text{m})$,相比基体的磨损量和磨损率降低了约为 78.9%;铁基和镍基合金熔覆层的磨损率相比基体分别降低了 52.6% 和 31.6%。由此可见,车轮钢表面熔覆钴基合金熔覆层后可使材料的耐磨性得到大幅提升。

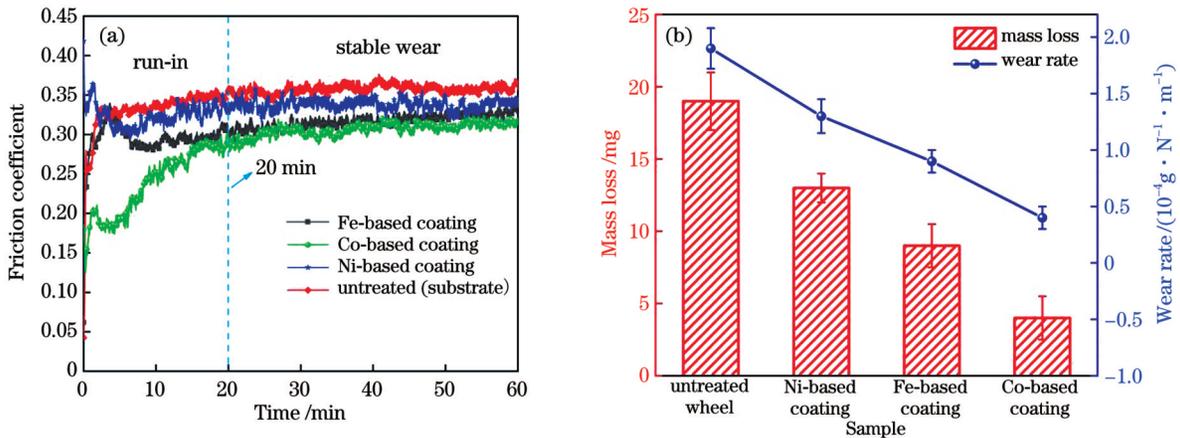


图 9 基体和熔覆层的摩擦磨损测试。(a)摩擦因数;(b)磨损量及磨损率

Fig. 9 Friction and wear experiments of substrate and laser cladding coatings. (a) Friction coefficient; (b) mass loss and wear rate

图 10 为各试样三维磨损形貌与最大磨损深度的对比图,其中的二维横截面轮廓图为各试样磨损区中部轮廓。由三维形貌图可以发现,铁基和钴基熔覆层试样的表面是比较平整的,镍基熔覆层试样的磨损表面上出现了许多相互平行的沟槽,基材试样的磨损表面上出现了“凸峰”(这些凸峰主要是摩擦过程中表面颗粒脱落形成的磨屑堆积而成的)。从磨损深度来看,4 种试样对应的最大磨损深度分别为 $16.37 \mu\text{m}$ (铁基熔覆层试样)、 $17.03 \mu\text{m}$ (镍基熔覆层试样)、 $10.70 \mu\text{m}$

(钴基熔覆层试样)和 $30.06 \mu\text{m}$ (基材)。显然,钴基熔覆层试样的最大磨损深度最小且磨痕宽度最窄,说明钴基合金熔覆层的耐磨性最优。结合前述微观组织及硬度的分析结果可知,钴基合金熔覆层的组织细小且均匀,其表面形成的大量碳化物弥散分布于晶体和晶间起到的弥散强化与固溶强化的双重强化效果较铁基和镍基合金熔覆层表面的强化效果更好,且其硬度较高,可以在很大程度上提高材料表面的耐磨性。

图 11 为各熔覆层与基体表面的磨损形貌。铁基

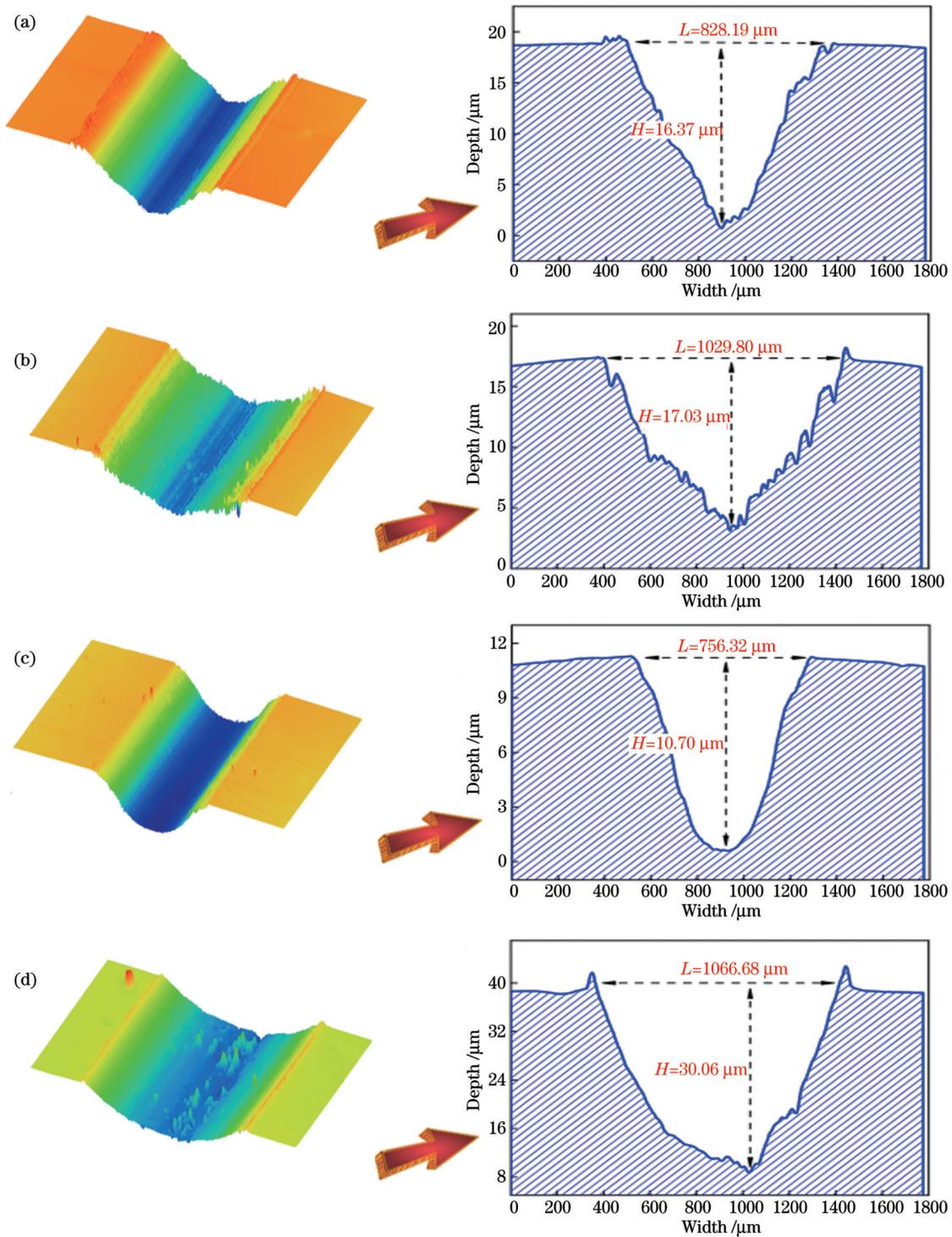


图 10 试样的三维磨损轨迹与最大磨损深度。(a)铁基熔覆层;(b)镍基熔覆层;(c)钴基熔覆层;(d)基体

Fig. 10 Three-dimensional wear trajectory and maximum wear depth of samples. (a) Fe-based laser cladding coating; (b) Ni-based laser cladding coating; (c) Co-based laser cladding coating; (d) substrate

合金熔覆层磨损表面出现了轻微的分层现象,而且出现了明显的犁槽。这是由于硬度较高的铁基合金接触界面之间存在较大的切向力,因此表层出现了剥层现象^[10]。铁基合金熔覆层的磨损机制以磨粒磨损为主,并伴有少量黏着磨损特征。由图 12(a)所示的EDS能谱分析可知点1处磨屑中Fe和O元素的质量分数分别为43.09%和34.77%,说明磨损表面上的磨屑基本

上是氧化物。镍基合金熔覆层磨损表面粗糙并有大量块状和颗粒状磨屑堆积。剧烈磨损过程中的往复挤压促使表面材料出现块状磨屑,而剥落的碎片在剪切力作用下形成颗粒状磨屑^[38],说明这是磨粒磨损与黏着磨损耦合作用的结果。根据图 12(b)所示的磨屑的EDS分析结果可知氧化层中富集了大量O元素,说明高载下的持续摩擦导致磨损表面发生了氧化。钴基合

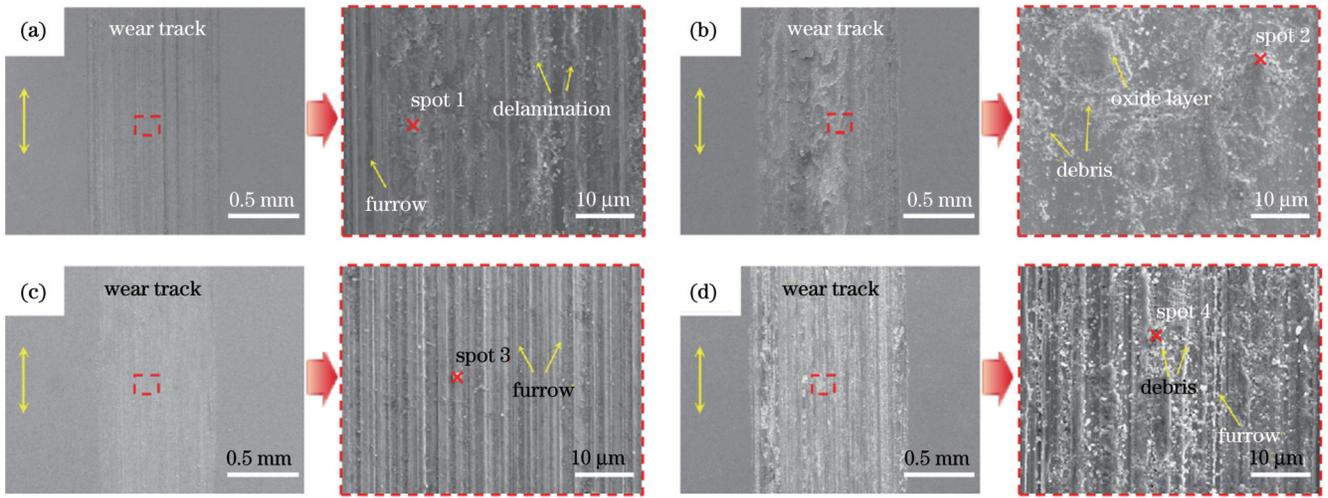


图 11 试样磨损区域的表面形貌。(a)铁基熔覆层;(b)镍基熔覆层;(c)钴基熔覆层;(d)基材

Fig. 11 Surface images of worn area of each sample. (a) Fe-based laser cladding coating; (b) Ni-based laser cladding coating; (c) Co-based laser cladding coating; (d) substrate

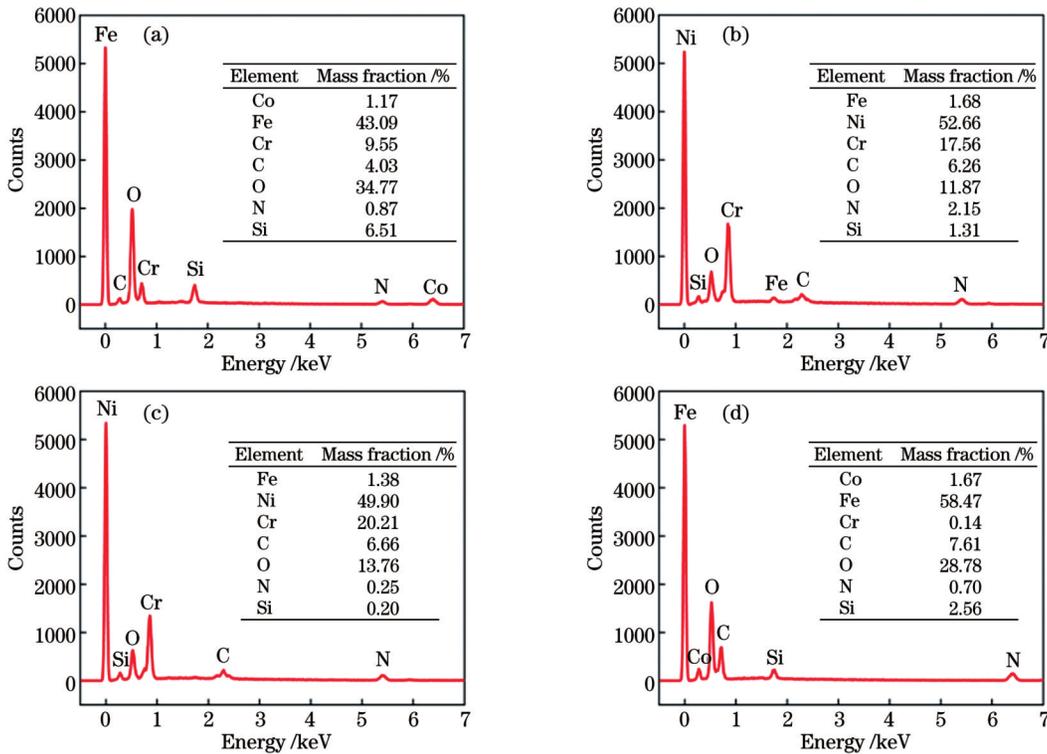


图 12 表面氧化物的EDS结果。(a)点1;(b)点2;(c)点3;(d)点4

Fig. 12 EDS results of surface oxides. (a) Spot 1; (b) spot 2; (c) spot 3; (d) spot 4

金熔覆层磨损表面主要出现了与滑动方向平行的犁沟,这是因为磨屑在接触载荷的加持下能够对表面造成压溃,而后在摩擦力作用下在表面留下大量犁沟^[39]。钴基合金熔覆层的磨损机制主要为磨粒磨损。由图 12(c)所示的钴基合金熔覆层磨屑的EDS分析可知点3处磨屑中Cr元素的质量分数高达20.21%,可以起到固溶强化作用,从而提升材料的抗塑性变形能力和抗磨损能力。基体的磨损较为严重,出现了犁皱纹且有大量磨屑随机分布。由图 12(d)所示的磨屑的EDS分析可知点4处磨屑中C元素的质量分数为

7.61%,说明从基体表面脱落的大量碳化物作为三体磨料对表面造成了严重磨损^[31]。基体的磨损机制是磨粒磨损与黏着磨损。综合对比基体和涂层试样的表面磨损情况可以发现,激光熔覆处理后涂层表面的磨损行为均得到了有效改善,其中钴基合金熔覆层表面的磨损最轻。

3.4 熔覆层的耐蚀性

图 13为基体和熔覆层试样在3.5%NaCl溶液中进行电化学阻抗测试得到的Nyquist图和Bode图。如图 13(a)所示,Nyquist曲线都呈现出容抗弧特征。容

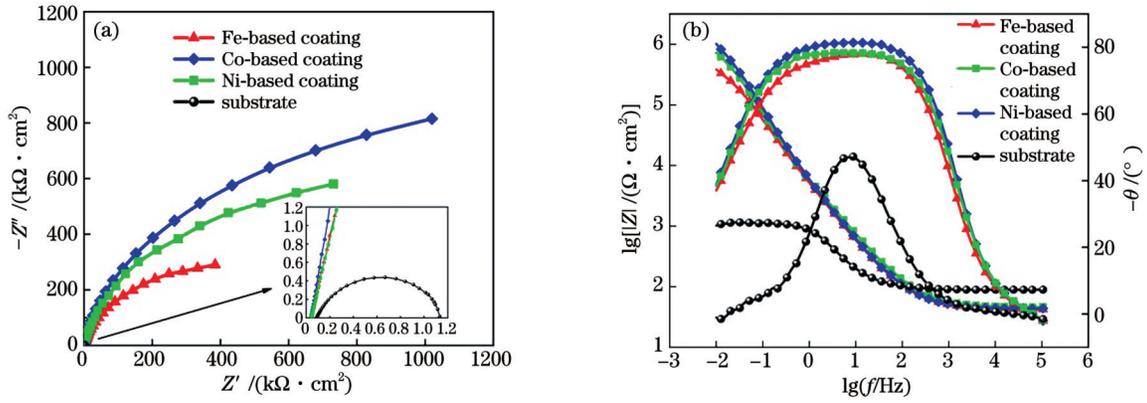


图 13 试样在 3.5%NaCl 溶液中的电化学阻抗谱。(a) Nyquist 图; (b) Bode 图

Fig. 13 Electrochemical impedance spectra of samples in 3.5% NaCl solution. (a) Nyquist diagram; (b) Bode diagram

抗弧的半径正比于耐蚀性^[40],即半径越大,耐蚀性越好。由此可以明显看出试样抗腐蚀能力从大到小依次是钴基熔覆层、镍基熔覆层、铁基熔覆层、车轮钢基材。由图 13(b)所示的 Bode 图可以看出激光熔覆试样的耐蚀性相比基体显著提高。最大阻抗值|Z|对应着各涂层抗腐蚀能力的强弱^[41],由图 13(b)可知钴基熔覆层具有最大的阻抗值。此外,各熔覆层在频率-相位角曲线中的中低频段均出现了一个宽峰,且相位角均为负数,说明各熔覆层试样在腐蚀过程中均表现为容性负载。

图 14 为建立的电化学等效电路图。在图 14(a)所示的基体的电化学等效电路中, R_s 为溶液电阻, R_{ct} 为腐蚀电荷转移电阻, CPE_{dl} 为非理想双电层电容^[42]。在图 14(b)所示的熔覆层的电化学等效电路中, R_f 和 CPE_{bl} 分别为熔覆层表面的钝化膜电阻和钝化膜电容。 R_{ct} 值越大,说明材料的耐蚀性越强^[43]。采用

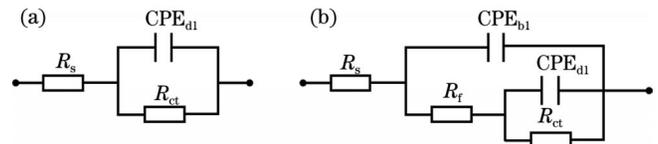


图 14 等效电路。(a) 基体; (b) 熔覆层

Fig. 14 Equivalent circuit. (a) Substrate; (b) laser cladding coatings

Zview 软件对阻抗谱进行拟合,拟合结果如表 3 所示,其中的 n 表示弥散指数 ($0 \leq n \leq 1$, 表征钝化膜的表面形态)。由表 3 可知,车轮钢基体的电荷转移电阻 R_{ct} 最小 ($0.74 \text{ k}\Omega \cdot \text{cm}^2$),而钴基熔覆层的腐蚀电荷转移电阻 R_{ct} 最大 ($535.89 \text{ k}\Omega \cdot \text{cm}^2$),大于镍基熔覆层 ($288.14 \text{ k}\Omega \cdot \text{cm}^2$) 与铁基熔覆层 ($135.55 \text{ k}\Omega \cdot \text{cm}^2$)。这一结果表明各熔覆层的耐蚀性优于车轮钢基体,且钴基合金熔覆层具有最优的耐蚀性。

表 3 熔覆层与基体的电化学阻抗拟合结果

Table 3 Electrochemical impedance fitting results of cladding layers and substrate

Sample	$R_s / (\Omega \cdot \text{cm}^2)$	$CPE_{bl} / (\mu\text{F} \cdot \text{cm}^{-2})$	n_{bl}	$R_f / (\text{k}\Omega \cdot \text{cm}^2)$	$CPE_{dl} / (\mu\text{F} \cdot \text{cm}^{-2})$	n_{dl}	$R_{ct} / (\text{k}\Omega \cdot \text{cm}^2)$
Fe-based coating	41.89	9.12	0.8832	25.5	23.62	0.2424	135.55
Ni-based coating	43.87	6.74	0.8945	1103.1	101.12	1.2760	288.14
Co-based coating	45.54	5.46	0.9145	1186.2	11.97	1.0340	535.89
Substrate	45.90				220.99	0.8313	0.74

为了进一步研究试样的耐蚀性,进行了动电位极化试验,试验结果如图 15 所示。可以看出,车轮钢基体在 3.5%NaCl 溶液中表现出活性溶解的特性,而各熔覆层均存在明显的钝化现象。同时可以发现熔覆层的自腐蚀电位 E_{corr} 相较于基体正移,而且各熔覆层按 E_{corr} 值从大到小排序依次为钴基熔覆层、镍基熔覆层、铁基熔覆层与基体。基于极化曲线,采用 Tafel 外推方法计算自腐蚀电位和自腐蚀电流密度 (J_{corr}),计算结果如表 4 所示。由表 4 可知,基体具有最小的 E_{corr} (-0.518 V) 与最大的 J_{corr} ($53.974 \mu\text{A}/\text{cm}^2$),而钴基熔覆层具有最大的 E_{corr} (-0.408 V) 与最小的 J_{corr} ($0.172 \mu\text{A}/\text{cm}^2$)。由此可见,在 3.5%NaCl 溶液中,熔覆层的腐蚀倾向与腐

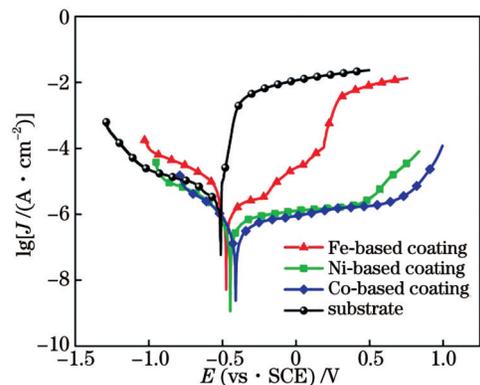


图 15 试样在 3.5%NaCl 溶液中的极化曲线

Fig. 15 Polarization curves of samples in 3.5% NaCl solution

蚀速率都远低于车轮钢基材,尤其是钴基合金熔覆层的耐蚀性显著优于基体。文献[44-46]指出,铬含量高的涂层在腐蚀过程中能形成良好的钝化层,从而增强其抗腐蚀能力,这与本文阻抗谱测试所得结果一致。

表 4 熔覆层与基体的极化参数

Table 4 Polarization parameters of cladding layers and substrate

Sample	$E_{\text{corr}} / \text{V}$	$J_{\text{corr}} / (\mu\text{A} \cdot \text{cm}^{-2})$	Corrosion rate / $(\text{mm} \cdot \text{a}^{-1})$
Fe-based coating	-0.475	2.980	0.035
Ni-based coating	-0.415	0.249	0.005
Co-based coating	-0.408	0.172	0.002
Substrate	-0.518	53.974	0.635

4 结 论

在 ER9 车轮材料表面制备了铁基、镍基和钴基合金熔覆层,研究了熔覆层的微观组织及性能,得到如下结论:

1) 车轮材料表面激光熔覆层的微观组织主要由枝晶组织和共晶组织构成;铁基熔覆层主要由 $\alpha\text{-Fe}$ 、 (Fe, Ni) 、 Cr_7C_3 等固溶体组成,镍基熔覆层主要由固溶体 $\gamma\text{-Ni}$ 、金属间化合物 FeNi_3 和硬质相 Cr_{23}C_6 组成,钴基涂层的结晶相主要是 FeNi_3 相、 $\gamma\text{-Co}$ 相和 Cr_{23}C_6 相。

2) 激光熔覆处理后,铁基熔覆层的显微硬度显著提升至 716.5 HV 左右,镍基和钴基合金熔覆层的硬度相比基体分别提高了 45.6% 和 72.8%。铁基熔覆层的伸长率和冲击韧性最低,塑性较差;钴基涂层的抗拉强度最大,约为 976.41 MPa;镍基涂层的伸长率约为 34.5%,冲击韧性高达 163.56 J/cm²,说明镍基涂层获得了良好的延展性。

3) 激光熔覆钴基合金涂层的摩擦因数(约 0.31)和磨损率[约 $0.4 \times 10^{-4} \text{ g}/(\text{N} \cdot \text{m})$]均最低,损伤最轻,磨损机制主要为磨粒磨损;铁基熔覆层的磨损率相比基体降低了 52.6%,其磨损机制以磨粒磨损为主,并伴有少量的黏着磨损特征;镍基熔覆层的磨损表面较为粗糙且存在磨屑堆积,其磨损机制为磨粒磨损与黏着磨损。

4) 铁基、镍基和钴基合金熔覆层在 3.5% NaCl 溶液中的电荷转移电阻分别为 135.55、288.14、535.89 $\text{k}\Omega \cdot \text{cm}^2$,均显著高于基体的电荷转移电阻,且钴基熔覆层具有最优的耐蚀性。

5) 对 3 种熔覆层进行比较及综合评价后可知,镍基熔覆层具有良好的塑韧性,但其耐磨性效果不佳,钴基熔覆层相对于铁基熔覆层具有更优异的耐磨和耐蚀性。在实际工程应用中,考虑到成本效益,铁基合金粉末仍为优选。

本文可为激光熔覆技术在车轮表面强化方面的工程应用提供一定的技术指导。

参 考 文 献

- [1] 王金能, 郭鑫, 敬霖, 等. 高速列车车轮踏面剥离引起的轮轨冲击力学响应有限元模拟[J]. 爆炸与冲击, 2022, 42(4): 151-165. Wang J N, Guo X, Jing L, et al. Finite element simulations of wheel-rail impact response induced by wheel tread spalling of high-speed trains[J]. Explosion and Shock Waves, 2022, 42(4): 151-165.
- [2] 朱爱华. 地铁车轮磨耗及其对动力学性能影响的研究[D]. 北京: 北京交通大学, 2020. Zhu A H. Study on the subway wheel wear and influence on dynamic performance[D]. Beijing: Beijing Jiaotong University, 2020.
- [3] 何柏林, 史建平, 颜亮, 等. 超声冲击对钢轨钢组织与性能的影响[J]. 中国铁道科学, 2009, 30(4): 58-62. He B L, Shi J P, Yan L, et al. The influence of the ultrasonic impact on the microstructure and properties of rail steel[J]. China Railway Science, 2009, 30(4): 58-62.
- [4] Zhang Y, Lian Q L, Wang X. Enhancement of rolling contact fatigue performance of ferrite-pearlite steel with laser shock peening[J]. Advances in Mechanical Engineering, 2019, 11(5): 1-9.
- [5] Meng L, Xian C, Zhu B B, et al. Comparison on the microstructure, bending properties and tribological behaviors of rail materials treated by laser dispersed quenching and induction assisted laser dispersed quenching[J]. Surface and Coatings Technology, 2021, 410: 126936.
- [6] Zhang Q S, Toda-Caraballo I, Dai G Z, et al. Influence of laminar plasma quenching on rolling contact fatigue behaviour of high-speed railway wheel steel[J]. International Journal of Fatigue, 2020, 137: 105668.
- [7] 余敏, 张鸿羽, 曹开, 等. 激光熔覆在高速列车上的应用研究现状[J]. 表面技术, 2020, 49(10): 12-20, 38. Yu M, Zhang H Y, Cao K, et al. Application status of laser cladding in high-speed trains[J]. Surface Technology, 2020, 49(10): 12-20, 38.
- [8] 孟丽. 钢轨表面激光-感应复合熔覆技术基础研究[D]. 武汉: 华中科技大学, 2019. Meng L. Fundamental studies of laser-induction hybrid cladding technique on full-scale rail surface[D]. Wuhan: Huazhong University of Science and Technology, 2019.
- [9] 丁昊昊, 慕鑫鹏, 祝毅, 等. 车轮材料表面 h-BN/CaF₂/Fe 基激光熔覆涂层组织与磨损性能[J]. 中国表面工程, 2021, 34(4): 139-148. Ding H H, Mu X P, Zhu Y, et al. Microstructures and wear properties of h-BN/CaF₂/Fe based laser claddings on wheel material surface[J]. China Surface Engineering, 2021, 34(4): 139-148.
- [10] 慕鑫鹏, 王文健, 祝毅, 等. 两种激光熔覆涂层对轮轨材料磨损与损伤性能的影响[J]. 摩擦学报, 2020, 40(2): 225-233. Mu X P, Wang W J, Zhu Y, et al. Effects of two laser cladding coatings on wear and damage properties of wheel/rail materials[J]. Tribology, 2020, 40(2): 225-233.
- [11] 慕鑫鹏. 车轮材料激光熔覆涂层微观组织与磨损性能研究[D]. 成都: 西南交通大学, 2020. Mu X P. Study on microstructure and wear properties of laser cladding coating on wheel materials[D]. Chengdu: Southwest Jiaotong University, 2020.
- [12] 丁阳喜, 邵晓峰, 袁颖群, 等. 高速车轮钢表面激光熔覆铁基合金涂层的摩擦磨损性能[J]. 材料保护, 2017, 50(4): 6-9, 19. Ding Y X, Shao X F, Yuan Y Q, et al. Friction and wear performance of laser cladding iron-based alloy coating on high-speed wheel steel[J]. Materials Protection, 2017, 50(4): 6-9, 19.
- [13] 丁阳喜, 张远昊, 邵晓峰. 激光熔覆层对轮轨滚动接触疲劳磨损性能的影响[J]. 热加工工艺, 2020, 49(2): 80-83. Ding Y X, Zhang Y H, Shao X F. Effects of laser cladding layers on wheel/rail rolling contact fatigue wear performance[J]. Hot

- Working Technology, 2020, 49(2): 80-83.
- [14] Guo H M, Wang Q, Wang W J, et al. Investigation on wear and damage performance of laser cladding Co-based alloy on single wheel or rail material[J]. Wear, 2015, 328/329: 329-337.
- [15] Ding H H, Mu X P, Zhu Y, et al. Effect of laser claddings of Fe-based alloy powder with different concentrations of WS_2 on the mechanical and tribological properties of railway wheel[J]. Wear, 2022, 488/489: 204174.
- [16] Wang W J, Fu Z K, Cao X, et al. The role of lanthanum oxide on wear and contact fatigue damage resistance of laser cladding Fe-based alloy coating under oil lubrication condition[J]. Tribology International, 2016, 94: 470-478.
- [17] Ringsberg J W, Franklin F J, Josefson B L, et al. Fatigue evaluation of surface coated railway rails using shakedown theory, finite element calculations, and lab and field trials[J]. International Journal of Fatigue, 2005, 27(6): 680-694.
- [18] Lewis S R, Lewis R, Goodwin P S, et al. Full-scale testing of laser clad railway track: case study-testing for wear, bend fatigue and insulated block joint lipping integrity[J]. Wear, 2017, 376/377: 1930-1937.
- [19] Zhu Y, Yang Y, Mu X, et al. Study on wear and RCF performance of repaired damage railway wheels: assessing laser cladding to repair local defects on wheels[J]. Wear, 2019, 430/431: 126-136.
- [20] 姜威. CrN/Ni60(WC)涂镀复合涂层组织和性能研究[D]. 兰州: 兰州理工大学, 2016.
Jiang W. Microstructure and property of flame sprayed and welded/PVD Ni60(WC)/CrN multilayer coatings[D]. Lanzhou: Lanzhou University of Technology, 2016.
- [21] 时晓宇, 温道胜, 王守仁, 等. 激光熔覆灰铸铁制动盘 Fe-Ni-Cr 梯度复合涂层微观组织及高温摩擦磨损性能研究[J]. 中国激光, 2022, 49(2): 0202017.
Shi X Y, Wen D S, Wang S R, et al. Microstructures and high-temperature friction and wear properties of laser clad Fe-Ni-Cr gradient composite coating for brake disc[J]. Chinese Journal of Lasers, 2022, 49(2): 0202017.
- [22] Li Y J, Dong S Y, Yan S X, et al. Phase evolution of ductile iron during laser cladding processing[J]. Surface and Coatings Technology, 2018, 339: 37-47.
- [23] 范鹏飞, 孙文磊, 张冠, 等. 激光熔覆铁基合金梯度涂层的组织性能及应用[J]. 材料导报, 2019, 33(22): 3806-3810.
Fan P F, Sun W L, Zhang G, et al. Microstructure, properties and applications of laser cladding Fe-based alloy gradient coatings[J]. Materials Reports, 2019, 33(22): 3806-3810.
- [24] Roy T, Lai Q, Abrahams R, et al. Effect of deposition material and heat treatment on wear and rolling contact fatigue of laser clad rails[J]. Wear, 2018, 412/413: 69-81.
- [25] He X M, Liu X B, Wang M D, et al. Elevated temperature dry sliding wear behavior of nickel-based composite coating on austenitic stainless steel deposited by a novel central hollow laser cladding[J]. Applied Surface Science, 2011, 258(1): 535-541.
- [26] 黄杰, 贺定勇, 杜开平, 等. FeCrNiMo 激光熔覆层组织与电化学腐蚀行为研究[J]. 表面技术, 2020, 49(12): 228-234.
Huang J, He D Y, Du K P, et al. Microstructure and electrochemical corrosion behavior of FeCrNiMo layer fabricated by laser cladding[J]. Surface Technology, 2020, 49(12): 228-234.
- [27] Lu J Z, Cao J, Lu H F, et al. Wear properties and microstructural analyses of Fe-based coatings with various WC contents on H13 die steel by laser cladding[J]. Surface and Coatings Technology, 2019, 369: 228-237.
- [28] Ma Q S, Li Y J, Wang J, et al. Investigation on cored-eutectic structure in Ni60/WC composite coatings fabricated by wide-band laser cladding[J]. Journal of Alloys and Compounds, 2015, 645: 151-157.
- [29] 童文辉, 赵子龙, 张新元, 等. 球墨铸铁表面激光熔覆 TiC/钴基合金组织和性能研究[J]. 金属学报, 2017, 53(4): 472-478.
- Tong W H, Zhao Z L, Zhang X Y, et al. Microstructure and properties of TiC/Co-based alloy by laser cladding on the surface of nodular graphite cast iron[J]. Acta Metallurgica Sinica, 2017, 53(4): 472-478.
- [30] Ren B, Zhang M, Chen C J, et al. Effect of heat treatment on microstructure and mechanical properties of stellite 12 fabricated by laser additive manufacturing[J]. Journal of Materials Engineering and Performance, 2017, 26(11): 5404-5413.
- [31] Li J J, Ju J, Chang W W, et al. Investigation on the microstructure and wear behavior of laser-clad high aluminum and chromium Fe-B-C coating[J]. Materials, 2020, 13(11): 2443.
- [32] 杨振, 柳宁, 樊湘芳, 等. 2Cr12NiMoWV 钢表面激光熔覆铁基合金组织及力学性能研究[J]. 应用激光, 2020, 40(1): 22-28.
Yang Z, Liu N, Fan X F, et al. Microstructure and mechanical properties of laser clad iron-based alloy on 2Cr12NiMoWV steel surface[J]. Applied Laser, 2020, 40(1): 22-28.
- [33] 王少杰, 韩靖, 曾伟, 等. 低温对 ER8 车轮钢力学性能的影响[J]. 材料研究学报, 2018, 32(6): 401-408.
Wang S J, Han J, Zeng W, et al. Effect of low temperature on mechanical properties of ER8 steel for wheel rim[J]. Chinese Journal of Materials Research, 2018, 32(6): 401-408.
- [34] 韩滨. CeO₂对模具表面激光熔覆 Fe 基复合涂层组织和性能的影响研究[D]. 济南: 济南大学, 2021.
Han B. Effect of CeO₂ on microstructure and properties of Fe-based composite coatings on die by laser cladding[D]. Jinan: University of Jinan, 2021.
- [35] 衡钊, 舒林森. 激光功率对 27SiMn 钢激光熔覆力学性能的影响[J]. 中国激光, 2022, 49(8): 0802011.
Heng Z, Shu L S. Effect of laser power on mechanical properties of laser clad 27SiMn steel[J]. Chinese Journal of Lasers, 2022, 49(8): 0802011.
- [36] 董月, 舒林森, 林冉. 激光熔覆 Fe-Cr-Mo-Si 合金涂层的组织与摩擦磨损性能[J]. 激光与光电子学进展, 2021, 58(19): 1914007.
Dong Y, Shu L S, Lin R. Microstructure and friction and wear properties of laser clad Fe-Cr-Mo-Si alloy coating[J]. Laser & Optoelectronics Progress, 2021, 58(19): 1914007.
- [37] 李聪玮. 27SiMn 钢表面激光熔覆铁基合金组织和性能研究[D]. 西安: 西安科技大学, 2021.
Li C W. Microstructure and properties of laser cladding Fe-based coatings on 27SiMn steel[D]. Xi'an: Xi'an University of Science and Technology, 2021.
- [38] 欧阳春生, 刘秀波, 罗迎社, 等. 304 不锈钢表面激光制备 Ti₃SiC₂-Ni 基自润滑复合涂层的高温摩擦学性能[J]. 表面技术, 2020, 49(8): 161-171.
Ouyang C S, Liu X B, Luo Y S, et al. High-temperature tribological properties of Ti₃SiC₂-Ni based self-lubricating composite coatings prepared on 304 stainless steel by laser cladding[J]. Surface Technology, 2020, 49(8): 161-171.
- [39] 刘正林. 摩擦学原理[M]. 北京: 高等教育出版社, 2009.
Liu Z L. Principles of tribology[M]. Beijing: Higher Education Press, 2009.
- [40] Chen J L, Zhou Y J, Shi C, et al. Microscopic analysis and electrochemical behavior of Fe-based coating produced by laser cladding[J]. Metals, 2017, 7(10): 435.
- [41] 王刚. Q345 表面激光熔覆镍基合金组织演化及性能研究[D]. 西安: 西安理工大学, 2021.
Wang G. Study on microstructure evolution and properties of laser cladding nickel-based alloy on Q345 surface[D]. Xi'an: Xi'an University of Technology, 2021.
- [42] 倪晓杰, 张博文, 赵忠贤, 等. 激光熔覆 Mo₂NiB₂-Cr₇C₃ 复合陶瓷熔覆层组织结构与性能研究[J]. 表面技术, 2021, 50(5): 60-69.
Ni X J, Zhang B W, Zhao Z X, et al. Investigation on the microstructure and properties of the laser clad Mo₂NiB₂-Cr₇C₃ composite coatings[J]. Surface Technology, 2021, 50(5): 60-69.
- [43] Karuppasamy S S, Jeyaprakash N, Yang C H. Microstructure, nanoindentation and corrosion behavior of colmonoy-5 deposition on SS410 substrate using laser cladding process[J]. Arabian Journal

- for Science and Engineering, 2022, 47(7): 8751-8767.
- [44] Dennis J K. Nickel and chromium plating[M]. Boca Raton: CRC Press, 1993.
- [45] Fan L., Chen H Y., Dong Y H., et al. Wear and corrosion resistance of laser-cladded Fe-based composite coatings on AISI 4130 steel[J]. International Journal of Minerals, Metallurgy, and Materials, 2018, 25(6): 716-728.
- [46] Hermas A A., Morad M S. A comparative study on the corrosion behaviour of 304 austenitic stainless steel in sulfamic and sulfuric acid solutions[J]. Corrosion Science, 2008, 50(9): 2710-2717.

Microstructure and Properties of Laser Cladding Coatings for ER9 Wheel Materials

Yang Wenbin^{1,2}, Li Shiyu¹, Xiao Qian^{1*}, Yang Chunhui¹, Chen Daoyun¹, Liao Xiaoyong¹

¹State Key Laboratory of Performance Monitoring and Protecting of Rail Transit Infrastructure, East China Jiaotong University, Nanchang 330013, Jiangxi, China;

²Key Laboratory of Urban Rail Transit Intelligent Operation and Maintenance Technology & Equipment of Zhejiang Province, Zhejiang Normal University, Jinhua 321005, Zhejiang, China

Abstract

Objective Wheels and rails of high-speed trains are prone to severe damage, fatigue, and fracture damage on the wheel surface owing to wear, corrosion, strength reduction, fatigue cracking, and other reasons, thus affecting the stability and safety of train operation. The commonly used repair process to eliminate wheel surface defects causes material wastage and economic losses. To improve the service life of a wheel, laser cladding technology is used to prepare a cladding layer on the surface of a wheel and rail to enhance their damage resistance. Therefore, in this study, Fe-, Ni-, and Co-based alloy coatings, widely used in the field of laser cladding, are prepared on the surface of the ER9 wheel material using laser cladding technology. The mechanical properties, damage mechanism, and corrosion behavior of the substrates and coatings are investigated.

Methods The base material of the laser cladding experiment was taken from the ER9 wheel steel tread, and three types of self-fluxing alloy powders—Fe-, Ni-, and Co-based—were used as cladding materials. Laser cladding technology was used to prepare the powder coating with thickness of 15 mm on sample surface by coaxial powder feeding. All samples was cut using the wire-cutting method. First, after the prepared metallographic samples were corroded, a SU8010 scanning electron microscope (SEM) and X-ray diffractometer (XRD) were used to study the microstructure and phase of the cladding layer. The microhardness of the samples was measured with a Vickers hardness tester (Qness-Q60). The prepared tensile and impact specimens were then tested for mechanical properties using an MTS universal testing machine and a Charpy pendulum impact testing machine, respectively. Furthermore, the fracture morphologies of the tensile and impact specimens were observed by SEM. Next, the prepared friction and wear samples were characterized by an MFT-EC4000 tester, and the wear surface, wear debris morphology, and element content of the samples were characterized and analyzed using SEM and its accompanying EDS. An electronic balance scale with an accuracy of 0.1 mg was used to measure the average wear. Finally, potentiodynamic polarization curves (Tafel) and electrochemical impedance spectroscopy (EIS) of the samples were obtained using an electrochemical workstation in a 3.5% NaCl solution at room temperature.

Results and Discussions As shown in Fig. 2, the coating surface is uniform and dense, without noticeable cracks, pores, and other defects. Furthermore, the microstructure is mainly composed of dendrites and eutectic structures. XRD spectrum analysis (Fig. 3) shows that the Fe-based coating is mainly composed of α -Fe, (Fe, Ni), Cr_7C_3 , and other solid solutions. The Ni-based coating is mainly composed of solid solution γ -Ni, intermetallic compound FeNi_3 and hard Cr_{23}C_6 phase. The crystal phases of the Co-based coating are mainly the FeNi_3 , γ -Co, and Cr_{23}C_6 phases. The investigation of mechanical properties indicates that the surface hardness after laser cladding treatment improves significantly (Fig. 4), and the Fe- and Ni-based alloy coatings have the highest microhardness (approximately 716.5 HV). The average hardness of the Ni-based alloy coating and Co-based alloy coating is approximately 384.2 HV and 456.1 HV, which are an increment 45.6% and 72.8%, respectively. The hardness of the coating structure is enhanced to achieve a strengthening effect. Figures 5 and 6 show that the elongation of the Fe-based tensile specimen is the lowest (1.34%), and the tensile fracture has cleavage steps. The tensile strength of the Co-based alloy coating is the highest (approximately 976.41 MPa), and the tensile fracture exhibits a river pattern feature. The tensile strength of the Ni-based alloy coating tensile specimen (approximately 813.95 MPa) decreases compared with the substrate, but the elongation reaches 34.5%, and the tensile fracture exhibits a dimple-like morphology. Figure 7 shows that the impact fractures of Fe- and Co-based coatings are brittle, while the Ni-based coating exhibits good ductility and an impact toughness considerably higher than that of the former two. In terms of friction and wear research (Figs. 9 and 11), the wear amount and wear rate of the coatings are significantly reduced, while those of the Co-based alloy coating are the lowest [4 mg and 0.4×10^{-4} g/(N·m), respectively], which is 78.9% lower than that of the base material. Only furrows appeared on the wear surface. The wear mechanism is mainly abrasive wear. The wear rate of the Fe-based alloy coating was reduced by approximately 52.6% compared with the substrate, and the wear surface is slightly damaged. The

wear mechanism is characterized by abrasive and adhesive wear. The Ni-based alloy coating has a rough grinding surface and a large amount of wear debris accumulation because of the coupling effect of abrasive and adhesive wear. In the electrochemical corrosion study, the Nyquist curves of the substrate and cladding layer in a 3.5% NaCl solution showed capacitive arc characteristics (Fig. 12). The maximum impedance of the cladding layer is two orders of magnitude higher than that of the substrate. According to the test parameters of the polarization curve (Table 4), the self-corrosion potentials of the Fe-, Ni-, and Co-based coatings are -0.475 , -0.415 , and -0.408 V, respectively, and the self-corrosion densities are 2.980, 0.249, and $0.172 \mu\text{A}/\text{cm}^2$, respectively.

Conclusions The microstructure of the laser cladding coating on the surface of the wheel material is mainly composed of dendritic and eutectic structures. The hardness of the coating is significantly improved. The Ni-based alloy coating has good tensile strength and impact toughness, and the fracture is characterized by toughness, whereas the Co- and Fe-based alloy coatings have a brittle fracture; however, the difference is marginal. Compared with the matrix, the cladding coatings have a lower friction factor, wear rate, and better corrosion resistance, and the Co-based alloy coating has higher hardness (the microhardness was increased by 72.8%). The wear resistance of the Co-based alloy coating is the best (the friction factor is 0.31, the wear amount is approximately 4 mg, and the wear scar depth is $10.70 \mu\text{m}$). The corrosion resistance of the Co-based alloy coating is the best (the impedance value is two orders of magnitude higher than that of the substrate). A comparative analysis of the three coatings shows that the Ni-based coating has a rough surface, high wear rate, poor wear reduction effect, and weak hardness and strength. The wear and corrosion resistance of the Co-based coating is higher than that of the Fe-based coating, but the latter has lower engineering costs and also provides overall wheel protection.

Key words laser technique; wheel material; laser cladding; alloy powder; microstructure; mechanical properties; wear resistance; corrosion resistance